

A numerical model of friction between rough surfaces

Yu. A. Karpenko, Adnan Akay *

Carnegie Mellon University, Mechanical Engineering Department Pittsburgh, PA 15213, USA

Received 2 March 1999; received in revised form 28 February 2000; accepted 9 May 2001

Abstract

This paper describes a computational method to calculate the friction force between two rough surfaces. In the model used, friction results from forces developed during elastic deformation and shear resistance of adhesive junctions at the contact areas. Contacts occur between asperities and have arbitrary orientations with respect to the surfaces. The size and slope of each contact area depend on external loads, mechanical properties and topographies of surfaces. Contact force distribution is computed by iterating the relationship between contact parameters, external loads, and surface topographies until the sum of normal components of contact forces equals the normal load. The corresponding sum of tangential components of contact forces constitutes the friction force. To calculate elastic deformation in three dimensions, we use the method of influence coefficients and its adaptation to shear forces to account for sliding friction. Analysis presented in Appendix A gives approximate limits within which influence coefficients developed for flat elastic half-space can apply to rough surfaces. Use of the method of residual correction and a successive grid refinement helped rectify the periodicity error introduced by the FFT technique that was used to solve for asperity pressures. The proposed method, when applied to the classical problem of a sphere on a half-space as a benchmark, showed good agreement with previous results. Calculations show how friction changes with surface roughness and also demonstrate the method's efficiency. © 2001 Elsevier Science Ltd. All rights reserved.

Keywords: Sliding contact; Surface roughness; Coefficient of friction

1. Introduction

Elastic deformation and adhesion are among the many different processes that contribute to resistance to relative motion during sliding contact [1,2]. The resistive forces on rough surfaces develop at the true contact areas between asperities. As surfaces slide against each other, different pairs of asperities come into contact. Location, size, and orientation of the contact areas, and the contact forces that develop at each, depend on asperity distributions, mechanical properties of the surfaces, external loads, and relative motion.

Progress of friction models between rough surfaces closely correlates with advances in experimental investigations of contact forces viz., [2–7] and theoretical modeling of surface roughness viz., [2,7–11]. Experiments show that shear stress at points of true contact (or local friction) depends on the contact pressure and in

most cases such a dependence is linear [2–4,7]. Interfacial shear stresses may result from a combination of shear resistance of adhesion [2,7] and contaminants in the interface [3,4]. However, studies also show that for rough surfaces adhesion usually has negligible effect on the contact area and pressure [5,6].

One of the pioneering attempts at using multi-asperity models to relate friction to elastic deformation and shear strength of adhesion dates back to the early works of Kragelsky [2]. He started with a surface model in which the asperities were considered as an assembly of rods of different length with their lower ends fixed in a rigid base. Applying a statistical approach, he expressed friction coefficient in a general form as a function of deformation behavior of surface material, height distribution of the rods, and the dependence of local friction on the contact pressure. For ease of analysis, Kragelsky assumed elastic rods that had linear height distribution, and that the local friction varied linearly with the contact pressure [2,7]. His analytical results showed an increase in coefficient of friction as surface roughness decreases, which agreed well with the corresponding experimental studies [1,2].

* Corresponding author.

E-mail address: akay@andrew.cmu.edu (A. Akay).

Modeling of surface roughness progressed with the study of contact of rough surfaces by Greenwood and Williamson (G–W) [8]. They assumed that surfaces are composed of hemispherically tipped asperities with a uniform radius of curvature. In accordance with the experimental observations, Greenwood and Williamson approximated the distribution of asperity heights about a mean plane as Gaussian [8]. For mathematical convenience, contact between two rough surfaces was simulated as a contact between an equivalent rough surface and a rigid flat plane. The equivalent rough surface is obtained by summing up the heights of the two real surfaces and by an effective modulus that represents their elastic moduli [8,12]. Whitehouse and Archard [9] extended the G–W model [8] by allowing for the random radii of curvature of the asperity tips. Nayak [10] introduced the techniques of random process theory into the analysis of Gaussian rough surfaces. He related surface statistics such as the distribution of summit heights, the density of summits, the mean surface gradient, and the mean curvature of summits to the power spectral density of a profile of the surface. Random process theory was also used by Bush et al. [11], who approximated the summits of surface asperities of random heights and curvatures by paraboloids with the same principal curvatures.

Francis generalized the asperity models described above to model sliding friction between rough surfaces [13]. By using Nayak's approach [10], he simulated Gaussian engineering surfaces with asperity shapes that are paraboloidal only at their vertices but otherwise have random heights and curvatures. To calculate elastic deformation at each asperity contact, Francis used the Hertz solution for elastic circular paraboloids [12]. To model the sliding resistance at true contacts, he utilized empirical relations based on data in [3,4]. By statistically summing over all asperity contacts, Francis expressed the total contact area, load, and the friction coefficient as functions of the separation of the mean surfaces.

Ogilvy removed the need for the simplifying assumptions about the geometry of asperities by presenting a numerical model to predict the friction force between rough surfaces [14]. The Ogilvy model considers contact between two numerically-generated Gaussian surfaces and also uses the concept of equivalent surface roughness [12]. Ogilvy calculated elastic deformation of asperities using the Hertz theory and accounted for their plastic deformation with a simple plasticity theory [1,14]. Under conditions of steady sliding [12], Ogilvy calculated friction force due to adhesion by using two methods that she called 'microscopic' and 'macroscopic.' When using the microscopic method, the total friction force becomes the sum of the adhesive forces required to break every junction [15]. In the macroscopic approach, the total friction force is related to the total true contact area under the assumption of constant shear

strength of adhesive junctions, but without considering the details of each asperity contact. Ogilvy observed a qualitative agreement between the numerical predictions of her model and corresponding experimental results [14].

The concept of equivalent roughness used in previous studies presumes that the true contact areas always have parallel orientation to the mean planes. To account for contacts at asperity slopes that may have arbitrary orientations [16,17], Ford developed a multi-asperity contact model [18]. He combined a previous model by Tabor [17, ch. 10] for a sliding contact point over triangular asperities with the statistical approach by Greenwood and Williamson [8] for frictionless contact between nominally-flat surfaces. By extending Ogilvy's method [14], Ford removed the restriction of asperity peaks to hemispherical shapes in the G–W model [8,18]. Ford showed that, for small asperity slopes, single asperity analysis [17] overestimates the influence of asperity slopes on friction compared with multiple-asperity contact analysis.

Other studies that address the problem of friction between rough surfaces include an extension of Tabor's model [17] by Seal [19] to the case where sliding is not along the principle slopes. Seal showed that experimentally observed anisotropy in friction may be explained by sideways excursions during sliding. Suh and Sin [20] found asperity deformations to be significant for static coefficient of friction but not in the case of sliding friction as compared with friction due to adhesion. In an investigation of the influence of roughness on rolling contact fatigue, Bailey and Sayles [21] considered contact between two-dimensional rough surfaces. They showed that presence of asperities within contact regions brings the maximum orthogonal and principal shear stresses to occur at or very close to the surface [21]. Hu et al. [22] extended the model in [21] to three-dimensional rough surfaces and showed that during steady sliding the amplitude and location of the maximum shear stress in the subsurface region continuously change. Tworzydło et al. [23] developed a constitutive model of contact interface by combining finite element analysis of surface asperities, empirical relations for local friction [3,4], and statistical homogenization techniques [10,13]. To validate their model, they measured sliding friction force between two rough surfaces made of steel and compared the friction coefficient obtained experimentally with its value predicted under assumptions similar to those in Ogilvy's macroscopic model of friction [14]. Based on an energy balance analysis at the interface of two-dimensional rough surfaces, Bengisu and Akay [24] related the interface forces to the relative normal and tangential velocities of contacting surfaces as a function of asperity deformation and adhesive shear forces. In another study [25], the same authors demonstrated how contacts at asperity slopes give rise to force components

in a direction normal to sliding and, thus, couple sliding and normal motions of the surfaces.

This paper describes a computational method to calculate friction force between three-dimensional rough surfaces under conditions of steady sliding [12]. The method assumes that friction results from elastic deformation of asperities and shearing of adhesive junctions. The model used here has two features that distinguish it from most of the previous ones: local friction depends on contact pressure [2–4,7], and contacts take place at the slopes of asperities and may have arbitrary orientations, similar to that developed by Bengisu and Akay [24,25].

The interdependence of contact forces and (size and slope of) contact areas makes it necessary to compute contact forces and areas iteratively. The method described below represents the relationship between a distribution of contact forces and the resulting displacement field by using the method of influence coefficients [12,26], originally developed for normal forces, adapted here to also include locally-tangential forces. The present method uses the empirical ‘binomial law’ of friction [2,7] to represent shear strength of adhesion at each contact instead of Coulomb’s law [21,22].

Use of a successive grid refinement technique [27] increases the computational efficiency of iterations in reaching a balance between normal components of contact and external forces. Details of the computational method are outlined later in the paper, followed by an example that demonstrates computation of friction parameters.

2. Description of the method

The contact model described below for sliding friction between two rough surfaces restricts itself to shallow asperities such that the rms value of their slopes is less than 0.1 rad [1,2]. In such cases, the interlocking effect that leads to shearing (fracture) of the asperities does not develop [2,20].

3. The contact model

The contact model described in this section considers two rough surfaces sliding [12] along a straight line parallel to the mean planes of the surfaces. The direction opposite that of sliding defines the tangential direction and the normal to the mean planes defines the normal direction of the coordinate system. The surfaces come into contact under the action of an external normal load, P . Fig. 1(a,b) portray an exaggerated cross-section of surfaces, designated as 1 and 2, just prior to and following contact. In both cases, the dotted lines represent the mean planes of the surfaces. Function $h(x,y)$ denotes the

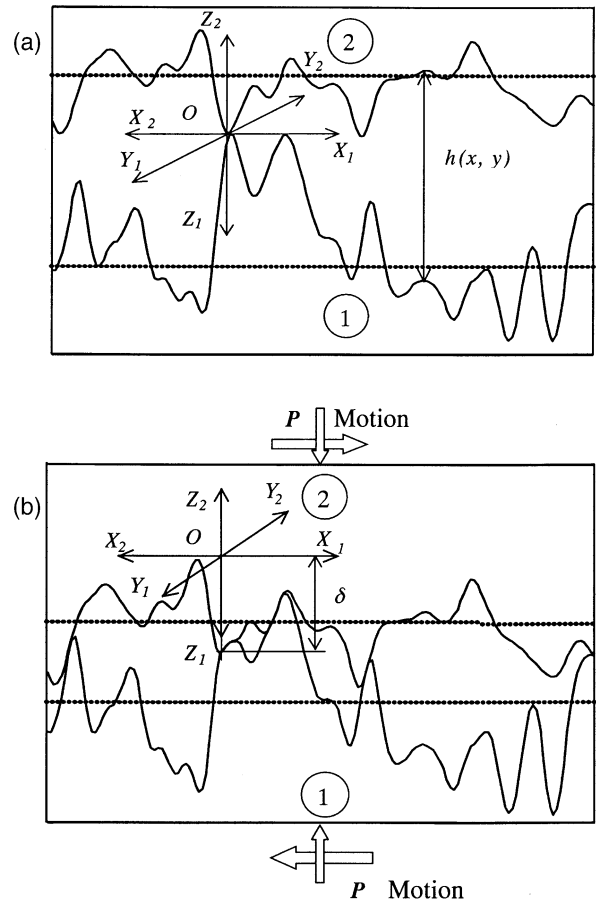


Fig. 1. Diagram of the rough surfaces: (a) before contact; (b) after deformation. Positions of the mean planes of half-spaces, (1) and (2), before and after deformation are shown with dotted lines.

separation between the two surfaces prior to deformation [Fig. 1(a)]. As shown in Fig. 1(b), δ represents the combined deformation of the surfaces at the first contact point¹. The plane parallel to the mean planes of the surfaces containing the point of first contact, O , establishes the plane of reference. The global coordinate axes for each surface have a common origin at O , with X_1 – Y_1 and X_2 – Y_2 planes that coincide with the plane of reference. The axes Z_1 and Z_2 , point away from the surfaces into the bodies [Fig. 1(a)].

The contact model used here only considers the contributions of forces developed at each asperity contact resulting from their elastic deformation and shear resistance due to adhesion. Under an applied normal load P , surface asperities come into contact and deform as

¹ As the maximum value of the combined deformation at each contact between the surfaces δ represents the approach between the surfaces.

depicted in Fig. 2(a), where dotted lines represent the undeformed shapes of the asperities and solid lines represent their deformed shapes. The model allows for true contacts between surfaces to take place at the slopes of their asperities, which may have arbitrary orientations (Fig. 1). Under such conditions, local normals at contact points do not necessarily coincide with the normal to the mean planes of the surfaces [24,25]; see Fig. 2(a). The corresponding spatial distribution of contact pressure, $f(x,y)$, that results from asperity deformation is represented schematically in Fig. 2(b).

The resistance of an adhesive junction to shearing takes place in the local tangential direction and, in effect, constitutes the local friction [24]. Following Kragelsky et al. [7], the shear stress due to local friction, r , is expressed with a binomial expression

$$r = \tau + \beta f, \tag{1}$$

where τ and β are empirical constants. For many metals and polymers $\beta = 0.02\text{--}0.25$; for metal–metal sliding

pairs $\tau = 2.5\text{--}30$ MPa and for metal–polymer pairs $\tau = 0.2\text{--}0.5$ MPa [7].

The aggregate of the normal components of deformation and local friction forces at all asperities throughout the contact region yields the normal force on the surfaces [24,25]; Fig. 2(b):

$$N = \iint_A (f \cos \theta_x - r \sin \theta_x) \cos \theta_y dx dy, \tag{2}$$

where A is the true contact area. The spatial derivatives, θ_x , and θ_y , of the deformed surfaces at contact points represent the contact slopes with respect to x and y directions in the global coordinate system. Under the assumption of quasi-static equilibrium, N must balance the load P . The corresponding sum of the projections of contact forces in the sliding direction constitutes the friction force, F :

$$F = \iint_A (f \sin \theta_x + r \cos \theta_x) \cos \theta_y dx dy, \tag{3}$$

and the friction coefficient, μ , is obtained from their ratio:

$$\mu = \frac{F}{P}. \tag{4}$$

Thus, the local friction and deformation forces each contribute to both vertical and tangential interface forces, N and F .

4. Computational method

The computational method described here utilizes the complex relationship that exists among external loads, material properties and topography of surfaces, and contact parameters. The contact parameters consist of contact forces, contact areas, and deformation at each contact. Their magnitudes, orientation, and distribution depend on external loads, and on the topography, or distribution, of asperities on the surfaces as described below.

Contact deformations on the surfaces collectively manifest themselves as the approach, or relative nominal deformation, between the surfaces. Thus, for any value of approach between the surfaces under external loads, there exists a corresponding distribution of contact forces, contact areas, and asperity deformations. Since at quasi-static equilibrium, local contact forces between surfaces balance the external loads on a friction pair, the relationship between external loads and contact parameters can be expressed in terms of approach δ [12]. The solution procedure described later iterates this relationship by adjusting the approach between the two surfaces until equilibrium is established between the external normal load P and the normal contact force N

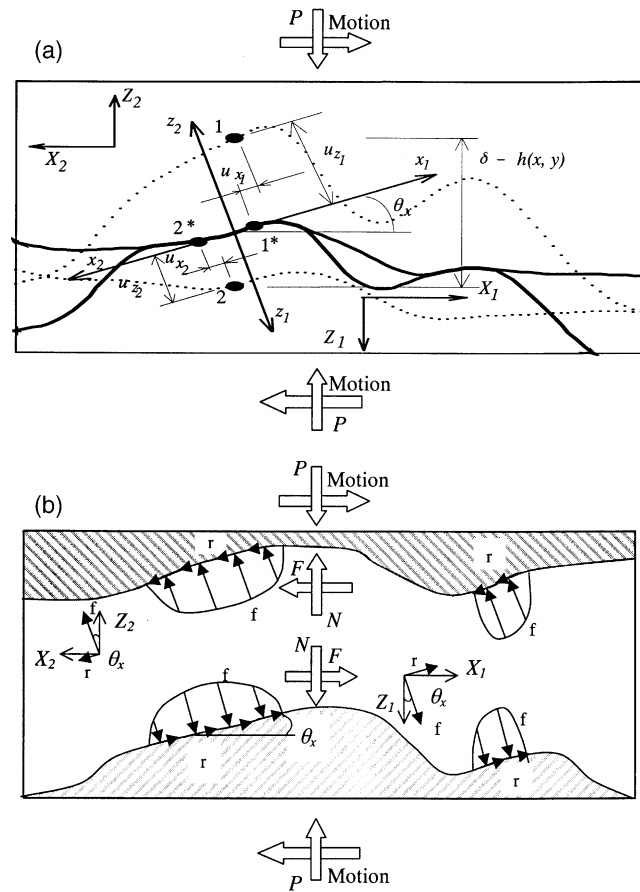


Fig. 2. Schematic description of asperities in contact (a) and the corresponding contact force distributions (b). Dotted lines represent undeformed shapes of the asperities. Solid lines represent their deformed slopes. Positions of the matching surface points before the contact and after the deformation are denoted with 1 and 2, and 1* and 2*, respectively, where $\delta - h(x,y)$ describes their contact approach.

$$P - N(\delta) = 0. \quad (5)$$

Following conventional contact analyses [12,21,26], we assume also that true contact area is contained within the kinematic interference area and that the relative tangential displacements are negligibly small. Then, the relationship between approach and local asperity displacements may be described geometrically as the kinematic interference of the surfaces, schematically shown in Fig. 2. As illustrated in Fig. 2(a), the local normal displacements $u_{z1}(x,y)$ and $u_{z2}(x,y)$ relate to the approach δ through the function $h(x,y)$:

$$u_{z1} + u_{z2} = [\delta - h(x,y)] \cos\theta_x \cos\theta_y, \text{ within contact area} \quad (6a)$$

$$u_{z1} + u_{z2} > [\delta - h(x,y)] \cos\theta_x \cos\theta_y, \text{ outside contact area} \quad (6b)$$

Because displacement at any point on an elastic surface depends on forces everywhere on the surface, calculation of local displacements requires consideration of both the normal and tangential forces at all contacts throughout the surface. However, contact forces themselves depend on displacement at the points of contact and, therefore, are not known a priori. Use of influence coefficients, which represent the relationship between displacement at a point and the forces that cause it [12,26], makes it possible to calculate normal displacements as a linear superposition of displacements due to forces at all contact points.

Two types of influence coefficients are necessary to calculate friction. In addition to the conventional influence coefficients that represent normal displacements $a(x,y)$ at any surface point due to a unit normal pressure acting over a grid element [26], influence coefficients representing normal displacements $c(x,y)$ due to a unit tangential traction, uniform over a grid element, are also required to model the effects of local friction [12]. Two complete sets of such influence coefficients for all grid elements, one set each for normal and shear tractions, constitute the corresponding flexibility matrices used for computations as described below.

Equations describing contact forces and the total field of local normal displacements are expressed in matrix form as:

$$[\mathbf{a}][\mathbf{f}] + [\mathbf{c}][\mathbf{r}] = [\mathbf{u}] \quad (7)$$

where $[\mathbf{u}]$ represents normal displacements due to all local normal and shear loads; $[\mathbf{a}]$ and $[\mathbf{c}]$ are the flexibility matrices due to locally normal and tangential tractions of unit intensity over each grid element, respectively. Matrices $[\mathbf{f}]$ and $[\mathbf{r}]$ represent the local contact pressure and local friction, where $[\mathbf{f}]$ is assumed to be positive inside the true contact area and to vanish outside

[12]. The local friction depends, in part, on the contact pressure, $[\mathbf{f}]$, and use of Eq. (1) makes it possible to represent their relationship as:

$$[\mathbf{r}] = \tau + \beta[\mathbf{f}]. \quad (8)$$

The computational method described here uses Eq. (7), along with Eq. (8), to obtain force distributions $[\mathbf{f}]$ and $[\mathbf{r}]$ for a given displacement field $[\mathbf{u}]$. Thus, the solution of Eq. (7) requires an initial estimate of $[\mathbf{u}]$, which is obtained here from the kinematic interference of the surface topographies.

Solving Eq. (7) first requires determining the flexibility matrices $[\mathbf{a}]$ and $[\mathbf{c}]$. Matrices of influence coefficients essentially define a set of Green's functions among the contact points. Analytical expressions for influence functions that describe force–displacement relationships exist only for an elastic half-space with a flat surface [12]. Although commonly used for rough surfaces as well [21,22,26], applicability of classical influence functions to oblique contacts has not been reported. The analysis described in Appendix A, based on analytical solutions of two related problems, gives approximate limits within which influence functions may be used for oblique contacts. The analysis in Appendix A combines the response in a half-space to a uniform pressure on a narrow strip of its flat boundary [12] with the response of an infinite wedge under arbitrarily distributed surface tractions [28]. As shown in Appendix A, influence functions for an elastic half-space are applicable to rough surfaces within limits. For the cases considered in this study where the rms value of asperity slopes varies between 0.125 and 2.5°, the analysis in Appendix A shows that the maximum error associated with the application of the conventional influence coefficients to rough surfaces is less than 2%.

5. Computational procedure

The computational procedure followed here consists of an iterative search for a value of δ that provides a global force balance between the external normal load and the sum of the normal components of contact forces [12,26]; Eq. (5). The process begins, as the first step, with the construction of matrices $[\mathbf{a}]$ and $[\mathbf{c}]$ in Eq. (7) with the use of a moving grid method described in [29]. Iteration consists of solving Eq. (7) for the distribution of local forces $[\mathbf{f}]$ and $[\mathbf{r}]$ for a given displacement field $[\mathbf{u}]$, initially estimated from kinematic interference of surfaces for an assumed value of approach δ ; Eq. (6a). The flexibility matrix $[\mathbf{a}]$ in Eq. (7) is inverted using an FFT-based technique [30].

For the computations, discretized rectangular traction elements represent the nominal contact area on each surface with $(M \times M)$ number of matching points located at

the center of each element viz., [12,22,26]. Each matching point has assigned to it a surface height relative to a selected datum. All traction elements and matching points are measured with respect to the global reference frame, which also acts as a reference frame for the influence coefficients in the flexibility matrices. A grid size with $M \times M$ traction elements results in a flexibility matrix of size $M_2 \times M_2$.

The solution process consists of three nested iterations described by a flow chart in Fig. 3. The first iteration determines, from among those identified by kinematic interference, the actual contact areas that have positive contact pressure. Because kinematically-based interference between surfaces does not account for their elastic deformation, the first iteration reconciles deformed surface geometry and contact forces. The second iteration seeks a balance between external normal load and the sum of the normal contact forces between the surfaces. The third iteration increases the resolution of contact areas by progressively decreasing the traction element size.

The solution process starts by bringing the surfaces together for an assumed value of approach where contact is detected through kinematic interference. Upon detection of contact, matrix $[\mathbf{u}]$ is constructed from the kinematic interference relations in Eq. (6a) for that particular value of approach δ . Eq. (7) is solved iteratively for $[\mathbf{f}]$ and $[\mathbf{r}]$ corresponding to the kinematically obtained contact displacements in $[\mathbf{u}]$ by using the flexibility matrix $[\mathbf{c}]$ and the inverse of matrix $[\mathbf{a}]$. At each iteration, those contact areas for which contact pressure is not positive are identified and excluded from the calculations [12,30]. Following convergence, the contact parameters still contain an error referred in literature as periodicity error [31,32]. This error results from the periodic extension of contact domain introduced implicitly into the contact analysis by Fourier transformation [31,32]. Assuming that such an error is equivalent to the residual of the solution vector $[\mathbf{f}]$, the method of residual correction is applied to Eq. (7) to modify the vector $[\mathbf{f}]$ so that its residual vanishes [27]. The first iteration thus yields distributions of contact areas, local friction and pressures that correspond to the assumed value of approach δ .

The second iteration adjusts the assumed value of δ until a balance is reached between the external normal load and sum of the normal components of all contact forces [12,26]. When balance is reached, (i) the corresponding δ represents the approach that would result from the applied load, and (ii) the sum of the corresponding tangential forces represents the friction force.

The third iteration improves the resolution of contact area distribution. In this iteration, however, to increase computational efficiency, results of the previous step with coarser grids, are interpolated using cubic polynomials for use with the new, higher-resolution elements. The solution process starts again with Eq. (7)

and continues until the desired convergence is achieved. Within this iteration, the computational effort to reach convergence is greatly reduced because the periodicity error introduced by FFT is already rectified.

For the computations reported below, the initial spatial resolution begins with a grid size of 128×128 for a 1.61×1.61 mm nominal contact area, followed by doubling it to 256×256 , and later quadrupled to 512×512 grids. The corresponding element sizes change from a ‘coarse’ 12.6×12.6 μm element to a ‘medium’ 6.3×6.3 μm element and finally to a ‘fine’ 3.15×3.15 μm element size. The results reported below are obtained using the fine mesh. The tolerances used for convergence are: $|\Delta[\mathbf{f}]/[\mathbf{f}]| \leq 10^{-5}$ and $|(P-N)/P| \leq 10^{-4}$.

The iterative computational method described above is applied in the next section to steady sliding of a sphere on an elastic-half-space to compare with previously reported analytical and numerical results [12,33].

6. Contact of a sphere with a flat surface

To validate the numerical method described above, we apply it to the case of a sphere sliding steadily on a half space. The choice of a sphere and half-space provides comparisons with previously reported analytical studies of frictionless contact [12,33] and numerical and experimental studies of roughness effects [2,7,14,18]. Choice of materials was motivated by the availability of empirical values for the coefficients τ and β in the binomial expression used for local friction, or resistance to shear of adhesive junctions [7].

6.1. Surface roughness

In the examples reported below, asperity height distribution, $\phi(z)$, and auto-correlation function, R_{zz} , characterize the statistical distribution of the numerically-generated roughness for each surface. Both surfaces have Gaussian height distributions and an isotropic ‘bell-shaped’ auto-correlation function (ACF) with a correlation radius of 104 μm that defines where the value of ACF reduces to 10% of its value at the origin [34]. These properties represent freshly ground surfaces [34].

For the computations, the asperity height distributions for the ball and the flat surface are normalized to have a unit rms value (or standard deviation) $\sigma=1$. This normalization makes it convenient to obtain actual height distributions for any surface with a different roughness amplitude by simply multiplying the normalized values with the desired value σ . The ACF is expressed in discrete form by

$$R_{zz}(k,m) = \sigma^2 e^{-2.3[k/l_x]^2 + m/l_y]^2} \quad (9)$$

where $k=0,1,2,\dots,l_x, m=0,1,2,\dots,l_y$, and l_x and l_y , represent

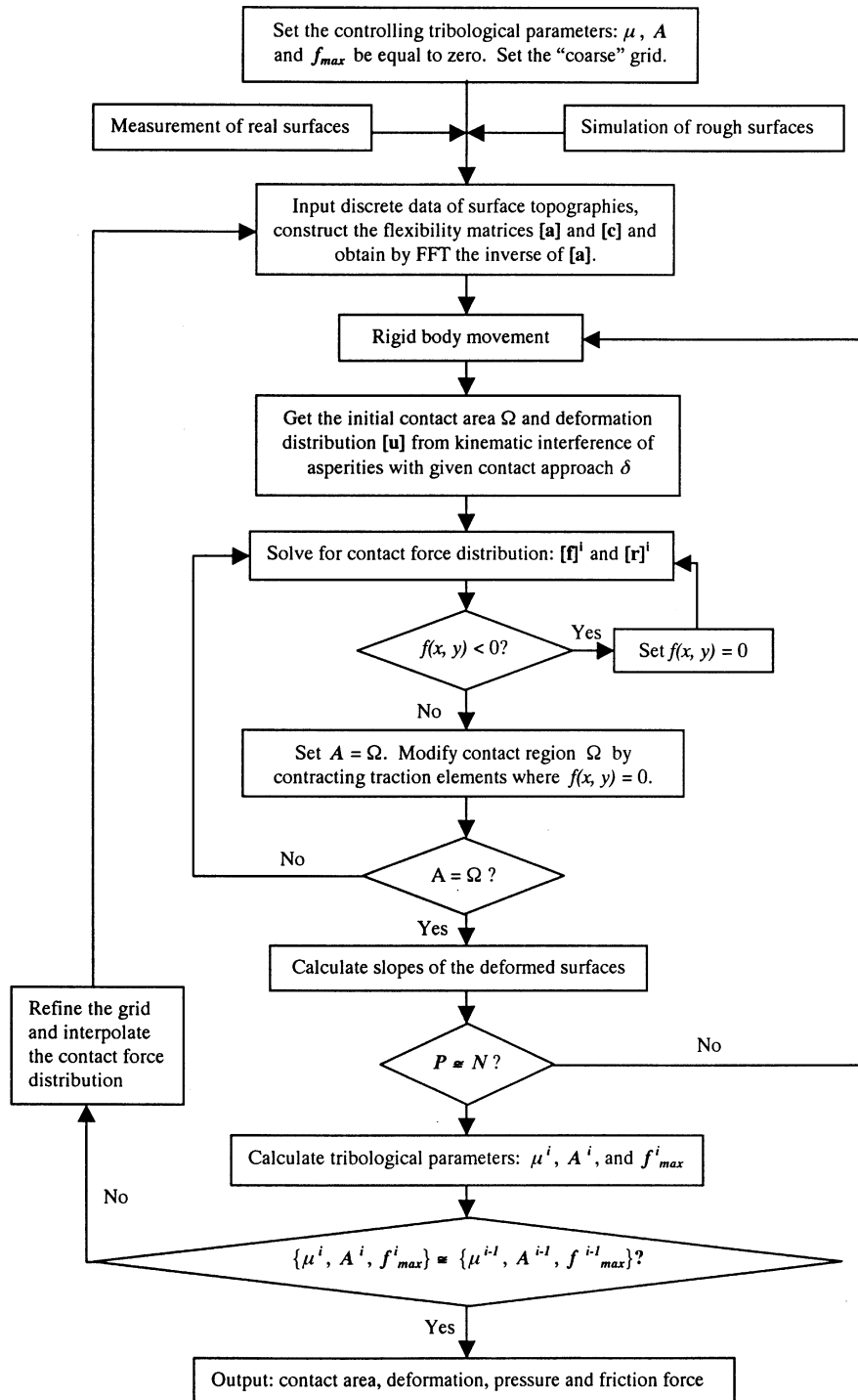


Fig. 3. Flow chart of the computer program that calculates iteratively sliding contact parameters between two rough surfaces.

the non-dimensional correlation lengths in x and y directions [35]. For the isotropic surfaces considered here, $l_x=l_y=l=33$.

In keeping with the established practice in the literature, roughness effects on friction and contact pressure are examined as a function of equivalent roughness, σ_e , of the two surfaces [12]. For the results reported below, a range of equivalent roughnesses is considered by com-

paring one surface roughness for the sphere with a series of surface roughnesses for the half-space. The roughness of sphere surface has standard deviations of $\sigma^{(s)}=0.084 \mu\text{m}$ for its asperity heights and $\sigma_{\theta_x}^{(s)}=\sigma_{\theta_y}^{(s)}=0.125^\circ$ for its slope distributions. Standard deviations for the flat surface roughness vary between $\sigma^{(fs)}=0.084$ and $1.680 \mu\text{m}$ for its asperity heights, and between $\sigma_{\theta_x}^{(fs)}=\sigma_{\theta_y}^{(fs)}=0.125$ and 2.50° for its slope distributions. Computations are car-

Table 1

Numerical values of the parameters used in calculations. The data for the binomial law of friction ($\tau=15$ MPa and $\beta=0.08$) are taken for a steel-copper pair [7]

Surface	$R(m)$	$E(GPa)$	ν
Ball	0.14	200	0.30
Falt	–	118	0.30

ried out for normal loads $P=14, 42, \text{ and } 70$ N. The empirical values for the coefficients in the binomial expression in Eq. (1) [7] and other relevant parameters used in the computations are given in Table 1.

Numerically generated rough surfaces (Fig. 4) used in the following computations have a spatial resolution of $\epsilon=3.15$ μm along both x and y directions. However, because ACF and height distribution together do not uniquely describe a surface topography, different sets of random inputs can lead to different surface representations while having the same statistical characteristics R_{zz} and σ [14,35]. As pointed out in earlier studies [14,18], such differences in surface representations lead to a variation in the values of the computed contact parameters. Thus, unless otherwise noted, the results reported below represent the average value of those that correspond to a set of 75 surface representations obtained using uncorrelated random inputs for given values of σ_ϵ and R_{zz} .

7. Model validation

Validation of the model described above consists of a comparison of numerical results with selected cases in the literature. The cases described below include simulation of steady sliding of a smooth sphere against a flat

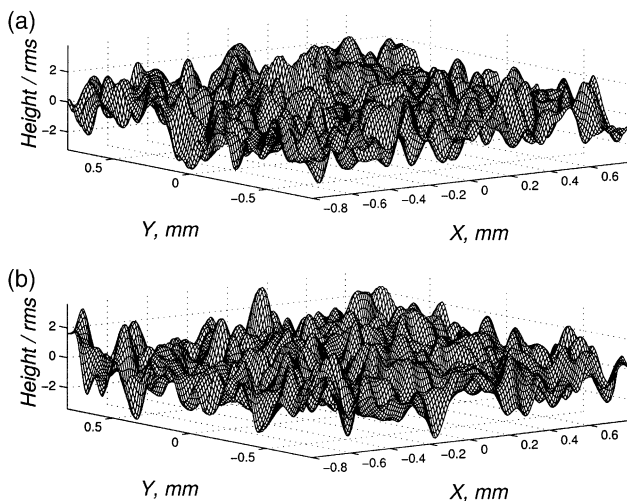


Fig. 4. Normalized surface roughness for the half-space (a) and the ball (b).

surface [12], ‘frictionless’ contact between a smooth sphere and a rough surface [12,33], and contact between two rough surfaces [2,7].

It is known that friction slightly shifts the pressure distribution and contact area between smooth surfaces of a ‘hard’ sphere and a more elastic half-space toward the trailing edge viz., [12]. Computations using Coulomb’s law of friction show a semi-elliptical distribution for the tangential contact stress similar in shape to the normal stress distribution, but reduced in amplitude in proportion to the friction coefficient. On the other hand, use of constant shear strength at the interface produces a uniform tangential stress across the contact area, independent of the normal pressure [14]. The binomial law of friction, Eq. (1), produces a tangential contact stress distribution as the sum of a constant shear stress τ distributed uniformly over the contact area and a Coulomb-like shear term, proportional to the contact pressure. Thus, near the edges of the contact area where contact pressure tends to zero, the Coulomb-like term also vanishes, leaving the adhesive shear stress τ to dominate the value of local friction (Fig. 5).

Frictionless contact refers to contact deformation in the absence of local friction. Greenwood and Tripp [33] examined the influence of roughness on contact pressure between a sphere and a half-space. They reported that the maximum value of the effective contact pressure is less than that of the Hertzian stress for the corresponding smooth surfaces. They further showed that, between rough surfaces, contact and contact pressure can exist outside the Hertz contact region calculated for smooth surfaces. By setting the constants τ and β in Eq. (8) to

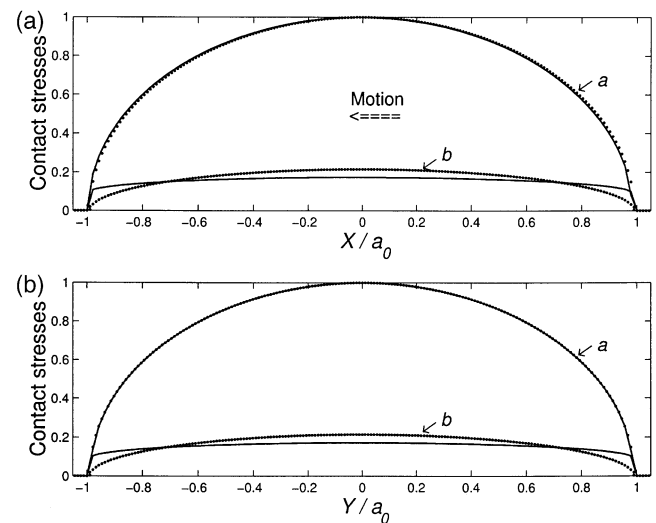


Fig. 5. Contact parameters between a sphere sliding against a half-space, both with smooth surfaces: (a) distribution of normal (a) and tangential stresses (b) in the sliding direction; (b) the corresponding distributions in the direction normal to the sliding direction. Dotted lines represent the distributions of the Hertzian contact stress and the tangential stress with Coulomb law of friction, where $P=70$ N.

zero and allowing contacts to take place only at the tips of asperities, the present method similarly simulates the effects of roughness on contact pressure distribution. Results presented in Fig. 6(a–c) show good agreement with those reported by Greenwood and Tripp [12,33]. An example of the distribution of pressure peaks between the rough surfaces (that exceed the maximum Hertz stress) illustrated in Fig. 6(d) also shows that pressure peaks may exist outside the Hertz region indicated by a_0 , radius of the Hertz contact area.

Computation of pressure distribution between two rough surfaces with and without local friction delineates what influence local friction, or shear strength of adhesion, may have on contact parameters. Results show that the local friction has negligible influence on contact deformation, which agrees with previously reported experimental results [2,7]. Fig. 7 portrays a cross-section of sphere and flat surface just prior to [Fig. 7(a)] and during contact [Fig. 7(b)], which illustrates the deformed asperities and deformed ‘mean plane’ of the flat surface. Deformed surface profile (dotted line) calculated by omitting shear adhesion maps nearly identically onto the profile obtained by including shear adhesion effects.

The benchmark cases considered provide a validation of the numerical method proposed here. In addition, results show that the combined deformation of asperities

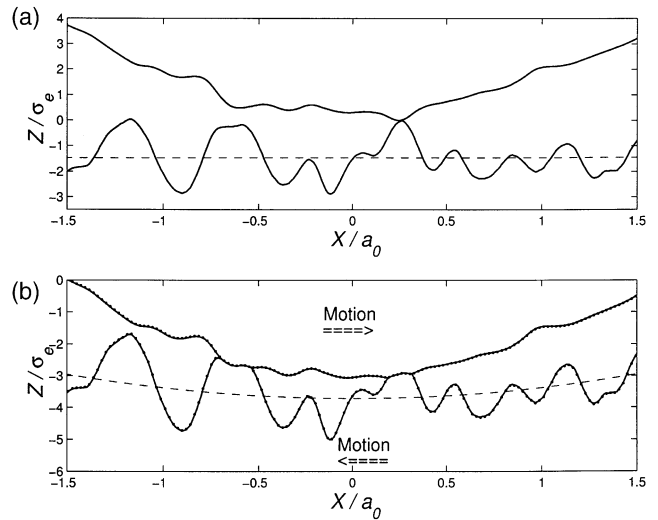


Fig. 7. Cross-section of the ball and half-space prior to contact (a) and in contact (b), where $P=70$ N and equivalent surface roughness $\sigma_e=0.511$ μm . The dashed line indicates the mean plane of the half-space; the dotted line—the contact deformation in the absence of friction.

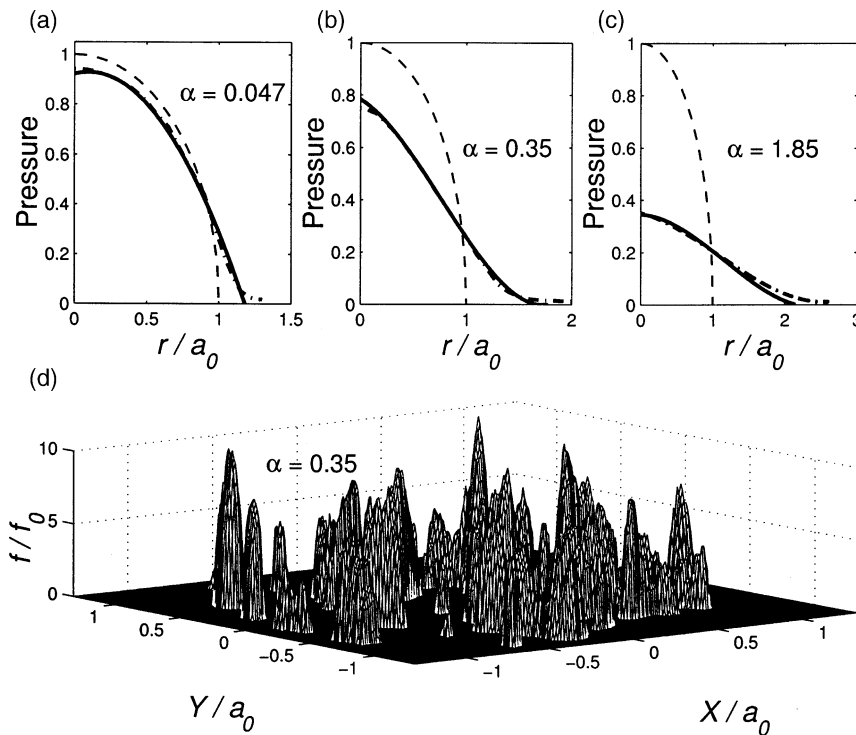


Fig. 6. Pressure distribution between a ball and a half-space with rough surfaces normalized with respect to the maximum Hertzian pressure f_0 between corresponding smooth surfaces, $f_0=163.9$ MPa: (a)–(c) effective pressure distributions when $\sigma_e=0.068$; 0.511 and 2.69 μm , correspondingly; (d) contact domain when the equivalent surface roughness $\sigma_e=0.511$ μm . Solid line—the present model; broken line—Hertz pressure, and dashed dotted line—the model by Greenwood and Tripp [12,33]. The radius of the Hertz contact $a_0=0.452$ mm; the parameter α is a ratio between the surface roughness σ_e and the bulk compression given by the Hertz theory, δ_0 [12].

and of the mean plane of the flat surface has a comparable magnitude to the average height of asperities. Consequently, the deformed contact areas may not have the same statistical characteristics they had prior to their deformation and, thus, they may no longer have a Gaussian distribution as discussed later.

8. Effects of roughness

Results show that surface roughness reduces friction in a complex manner. Friction coefficient μ , as shown in Fig. 8(a), decreases exponentially with increasing surface roughness. Its rate of change asymptotically approaches a constant value beyond $\sigma_e \cong 0.5 \mu\text{m}$, similar to results reported in [2,14]. As shown in Fig. 8(b), the total contact area changes with σ_e in the same manner as μ . Thus under constant load, the mean contact pressure, $f_m = N/A$, increases with roughness. Results in Fig. 8(c) show that, under constant load, friction coefficient and contact area both have nearly identical rates of change with respect to σ_e .

An explanation for the $\mu - \sigma_e$ dependence may be

given by extending the shear adhesion term in Eq. (1) to rough surfaces. Similar to the application by Singer [36] to smooth contact of ball bearings and flat surfaces, an analogous expression that approximates μ for rough surfaces may be obtained as follows. Substituting for r in Eqs. (2) and (3) and restricting in contact to the asperity tips ($\theta \cong 0$), friction coefficient can be written as:

$$\mu \cong \frac{\iint_A (\tau + \beta f) dx dy}{\iint_A f dx dy} = \frac{\tau A}{N} + \beta = \frac{\tau}{f_m} + \beta \tag{10}$$

At high contact pressures such that, $\tau/f_m \ll \beta$, β dominates the value of μ . In accordance with simple plasticity theory [1,14], the upper limit for the mean contact pressure may be represented by the hardness, H , of the softer material. Hence, the smallest value of μ (for small asperity slopes) may be approximated as:

$$\mu = \frac{\tau}{H} + \beta \tag{11}$$

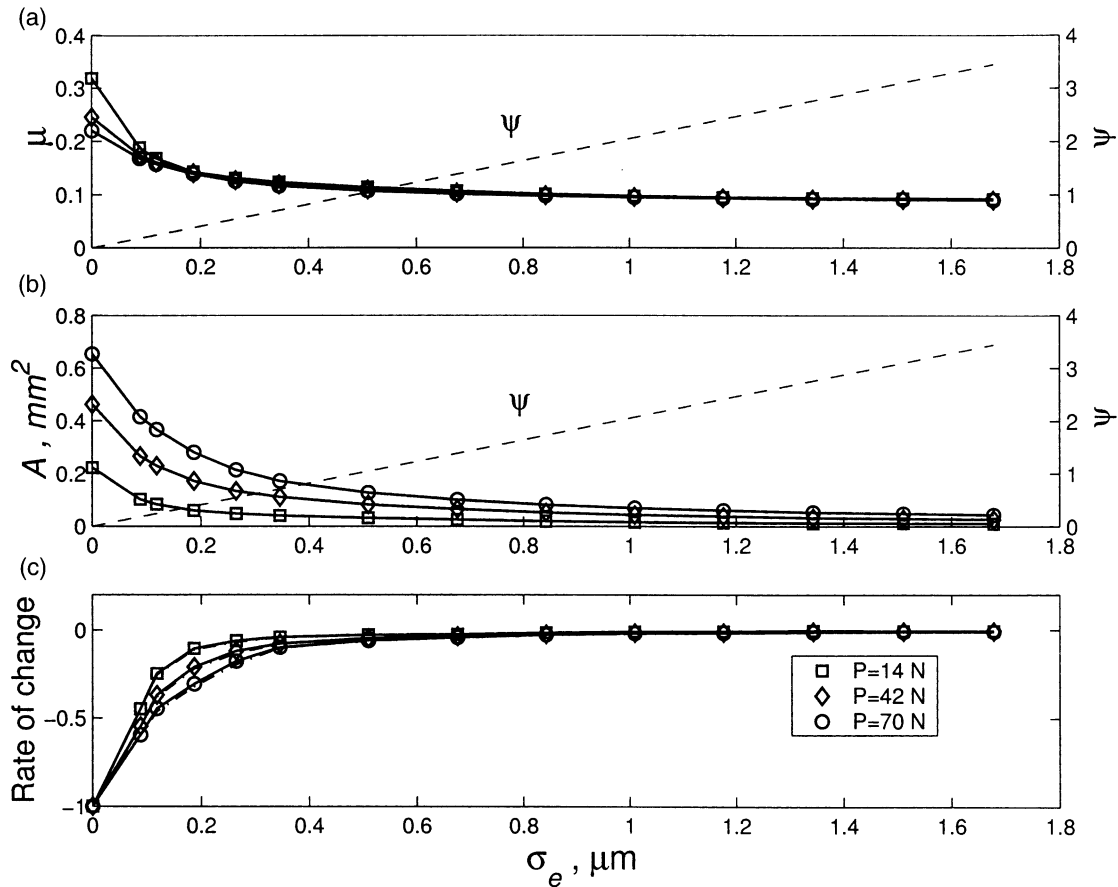


Fig. 8. Predicted variation of sliding contact parameters between a sphere and a half-space with their equivalent roughness σ_e and plasticity index ψ [8]: (a) variation of friction coefficient; (b) of contact area; (c) of their rates of change, where solid line— $d\mu/d\sigma_e/d\mu/d\sigma_e|_{\sigma_e=0}$, and dashed dotted line— $dA/d\sigma_e/dA/d\sigma_e|_{\sigma_e=0}$.

For the case considered here ($H_{Cu}=800$ MPa [7]), the lowest value μ reaches is estimated as 0.1. This result approximates well the asymptotic value μ reaches in Fig. 8.

Plasticity index ψ and its dependence on surface roughness [8] provides an explanation for the critical value of $\sigma_e=0.5$ μm about which friction becomes less sensitive to further increase in roughness. For Gaussian surfaces, ψ , may be approximated as [14]:

$$\psi \sim 2.2 \frac{E'}{H} \left(\frac{\sigma_e}{\epsilon} \right), \quad (12)$$

where E' is the effective elastic modulus [12]. As shown in Fig. 8, ψ reaches the threshold value of unity at about $\sigma_e \cong 0.5$ μm beyond which contact ceases to be purely elastic [8] and falls outside the conditions of the model used here. In such a case, Eq. (11) may be used to estimate the friction coefficient.

The variations in numerically generated surface descriptions, due to the differences in initial conditions described earlier, introduce fluctuations to μ through fluctuations in the contact area A . In the results presented in (Fig. 8), contact area A fluctuates by 7.5% about its mean value with a corresponding variation in μ of approximately 1.0%. The difference between the variations of contact area and friction results from the presence of a constant shear adhesion term β in Eq. (10). Computations with $\beta=0$ in Eq. (8) shows variation of μ to be the same as that for A , 7.5% the same order of magnitude as in [18] in which local friction was taken to be independent of contact pressure.

Results also show the existence of a binormal component Q of the contact forces (normal to the direction of motion in the tangential plane). As illustrated in Fig. 9,

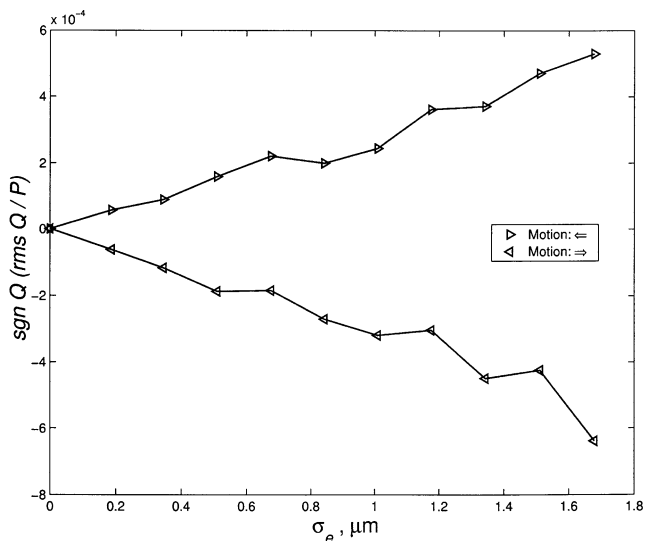


Fig. 9. Binormal component of the interface force Q (normal to the direction of motion in the tangential plane) between rough surfaces of a sphere sliding against a half-space, where $P=70$ N.

Q has a very small amplitude in comparison with that of the normal load P . Binormal force results from the deformation of asperities. Although it has a very small magnitude, in cases where high level of accuracy is required, binormal force may become important [19].

Compared with shear adhesion, forces resulting from elastic deformation of asperities have negligible direct contribution to the total friction force, as shown in Fig. 10(a). However, their indirect contribution to friction through adhesive forces makes elastic deformation a necessary part of the model and the computations.

In the cases considered here, both the total friction force and its component due to elastic deformation vary with the direction of relative motion, as observed previously [18]. As shown in Fig. 10, the difference, while very small in absolute terms, depends on surface roughness. The source of anisotropy of friction force, and its components, relates to the distribution of surface roughness within the contact areas. Although the asperity heights and slopes on undeformed surfaces both have Gaussian distributions, corresponding distributions within the much smaller set of true contact areas (that are now deformed) may no longer remain Gaussian. Results show that the distribution of the asperity heights and their slopes at contact areas differ from their original Gaussian distributions, as illustrated in Fig. 11. In particular, the distribution of deformed asperity slopes exhibits an overall negative skewness indicating a non-Gaussian feature, see Fig. 11(d).

The efficiency of the proposed approach compares favorably with those reported in the literature for static contact between a half-space and a sphere with a rough surface. Table 2 summarizes CPU times spent by using

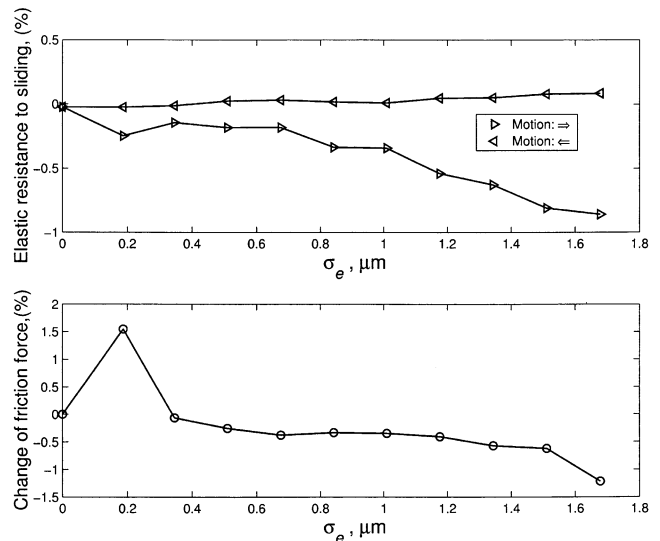


Fig. 10. Relative change in friction force due to the change in the direction of sliding of a sphere against a half-space, where $P=70$ N. The upper figure shows resistance to sliding due to elastic deformation force normalized with respect to friction force. The lower figure shows the relative difference between the total friction forces.

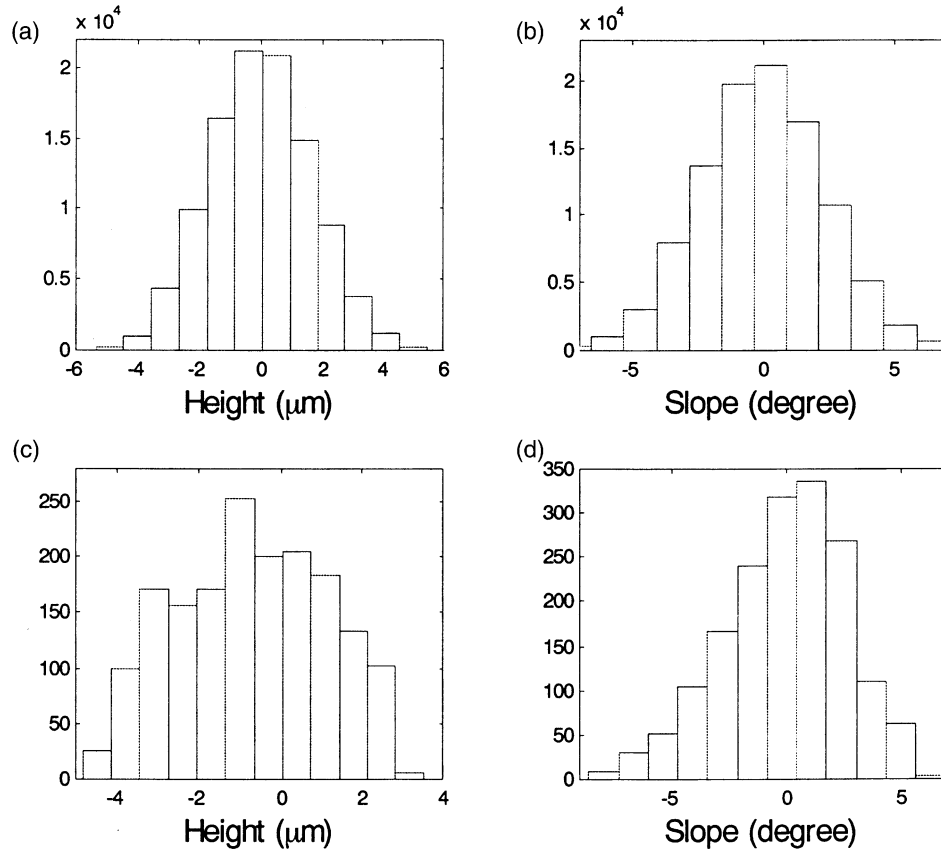


Fig. 11. Roughness distribution of undeformed and deformed flat surfaces, where $P=70$ N: (a) height distribution of undeformed surface in the region of the nominal contact area, $\sigma_y^{(s)}=1.680$ μm; (b) slope distribution of undeformed surface, $\sigma_\theta^{(s)}=2.5^\circ$; (c) height distribution of deformed surface at the real contact area, and (d) slope distribution of asperities in contact.

Table 2

Comparison of computing time between variational approach [37] and matrix inversion approach based on the developed computation technique. The specifications of the hardware: Silicon Graphics Indigo R-4000/100 MHz workstation (60.5 SPECfp92) [37] and PC with Pentium processor 90 MHz (70.5 SPECfp92). Cases 1–4 in our calculations correspond to the following set of grids: 100×100, 128×128, 256×256 and 512×512

Case	Matrix Inversion by FFT		Computing time	Variational principle [37]		Computing time
	Contact points Initial	Contact points Final		Contact points Initial	Contact points Final	
1	9801	1821	0.07 h	9717	1711	1 h
2	14697	4371	0.42 h	–	–	–
3	59171	17383	7.21 h	65310	16517	4 days
4	23715	68951	2.1 days	–	–	–

the present method and those by a variational approach as reported in [37] to solve for the true contact area and pressure, in both cases without local friction. Using the method described above, computations for contact area A , friction coefficient μ , and the maximum contact pressure f_{\max} converge up to two decimal places with the use of ‘fine’ mesh. Table 3 gives representative examples that show convergence of calculation results.

9. Summary

The computational method described in this paper calculates friction force by summing the forces that resist the relative motion at the true contact areas between two rough surfaces. The model for the resistive forces includes those due to local friction and elastic deformation. The size and location of true contact areas

Table 3
Numerical values of the tribological parameters calculated via successive grid refinement

$\sigma_{\text{half-space}}$ (μm)	0			0.504			1.008			1.680		
σ_{sphere} (μm)	0			0.084			0.084			0.084		
Parameters of the model	Mesh, $M \times M$											
	128	256	512	128	256	512	128	256	512	128	256	512
$A/10^{-1}$ (mm^2)	6.54	6.44	6.43	1.35	1.26	1.22	0.77	0.71	0.70	0.50	0.45	0.44
$\mu/10^{-1}$	2.20	2.19	2.18	1.09	1.07	1.06	1.01	0.97	0.95	0.94	0.91	0.89
$f_{\text{max}}/10^{-1}$ (GPa)	1.63	1.64	1.64	17.9	18.5	19.1	30.8	31.4	32.1	50.2	52.1	52.8

depend on the topography as well as on the contact forces that develop at each area. Arbitrary orientation of contacts at asperity slopes further complicates this interdependence between contact areas and forces. The resulting complex relationship is solved with an iterative technique. The solution process includes adapting the method of influence coefficients to shear forces.

Contacts at asperity slopes give rise to force components in both the sliding direction and normal to it, thus, coupling sliding and normal motions. Coupling of friction and normal forces has an important role in dynamic response of friction-excited systems. Use of pressure-dependent local friction and consideration of deformation of contacts at asperity slopes, set this model apart from the previous similar models. The numerical results presented above show dependence of friction on surface roughness and direction of motion. The reason for directional dependence is shown to be the non-Gaussian distribution of roughness within the contact region. It was shown that a surface with an undeformed Gaussian roughness distribution may have a non-Gaussian roughness distribution within the much smaller, non-contiguous true contact areas.

The present method handles the complexities associated with roughness of surfaces and oblique contacts efficiently using a nested iterative approach. The computational efficiency of the method outlined above is a favorable alternative to existing ones.

Acknowledgements

The authors wish to acknowledge helpful comments of the reviewers.

Appendix A

The purpose of the following analysis is to determine approximately the error associated in computing contact stresses on rough surfaces with the use of conventional influence functions developed for flat half-spaces. Corresponding analytical expressions that describe displacement distribution due to a unit force on a rough surface

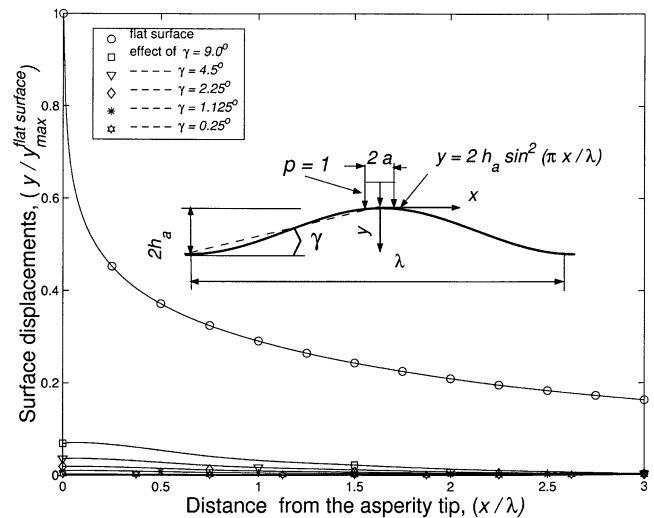


Fig. 12. Effects of surface waviness on surface displacement due to uniform pressure acting over the narrow strip on the boundary.

do not yet exist and their development is beyond the scope of this work. Similarly, direct numerical evaluation of such influence coefficients using theory of elasticity is too computationally intensive to be of practical use. The analysis presented below gives estimated limits of applicability by an approximate analysis.

As a first approximation, a one-dimensional sinusoidal profile describes surface roughness as illustrated in Fig. 12. To further simplify the analysis, a wedge tip on the flat half-space approximates each crest of the wavy surface (Fig. 13). The analysis begins by determining the effects of a periodic profile on surface displacement due to a uniform pressure acting over the narrow strip ($-a \leq x \leq a, a \ll \lambda$) on the flat boundary of the elastic half-space [12]. Simulating an asperity as a wedge tip can give its stress-strain field following the work of Tranter [28]. The analysis described here yields influence functions for a wedge tip by calculating displacements normal to the mean plane of the surface (y -direction) in response to a unit amplitude pressure applied on its faces near the tip (Fig. 13). Comparison of influence functions for a wedge tip with those for a flat surface [12] establishes approximately the error that results from using the

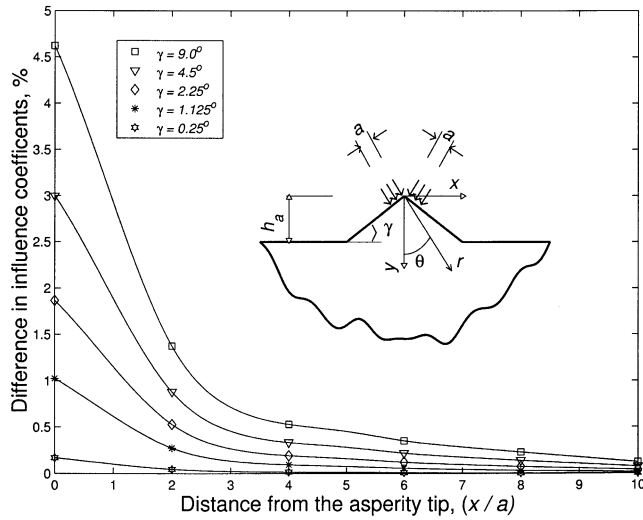


Fig. 13. Effects of simulated asperity on influence functions shown as relative differences in comparison to the conventional case of a flat surface.

conventional influence functions in calculating displacement on a rough surface.

The effects of surface roughness on the displacement field of a half-space are found by superposing a rough surface profile on the free flat surface in equations that describe the stress field in a half-space. The equations that represent the 2-D stress field produced by a uniform pressure having an intensity p per unit length along the z -axis and acting over the strip $(-a \leq x \leq a)$ are given by,

$$\sigma_x = -\frac{p}{2\pi} \{2(\theta_1 - \theta_2) + (\sin 2\theta_1 - \sin 2\theta_2)\} \quad (A1a)$$

$$\sigma_y = -\frac{p}{2\pi} \{2(\theta_1 - \theta_2) - (\sin 2\theta_1 - \sin 2\theta_2)\} \quad (A1b)$$

$$\tau_{yx} = \frac{p}{2\pi} (\cos 2\theta_1 - \cos 2\theta_2) \quad (A1c)$$

where $\tan \theta_{1,2} = y/(x \mp a)$, $-\infty < x < \infty$, and $0 \leq y < \infty$, [12]. A sinusoidal surface profile describes the roughness of the surface

$$y = 2h_a \sin^2 \frac{\pi x}{\lambda} \quad (A2)$$

where the amplitude h_a represents an asperity height and is much smaller than the wavelength $h_a \ll \lambda$. Substitution of (Eq. A2) into (Eq. A1a) gives a first-order approximation of the stress field, $\bar{\sigma}_x$, $\bar{\sigma}_y$ and $\bar{\tau}_{xy}$ on the sinusoidal surface.

A stress-free boundary on such a periodically wavy surface requires *pseudo* surface forces \bar{X} and \bar{Y} to compensate for the fictitious boundary stresses which the periodic profile of the surface induces,

$$\begin{aligned} \bar{X} &= -(\bar{\sigma}_x \cos \theta + \bar{\tau}_{xy} \sin \theta) \\ \bar{Y} &= -(\bar{\sigma}_y \sin \theta + \bar{\tau}_{xy} \cos \theta) \end{aligned} \quad (A3)$$

where θ is the slope of the boundary.

Surface displacements due to the pseudo forces are calculated as a function of surface waviness and compared in Fig. 12 with those due to a strip loading of the flat half-space. Not surprisingly, the effect of surface waviness is smaller for shallower waviness amplitudes. Of particular interest in these results is the confinement of displacement to within the tip of the asperity which suggests that it may be permissible to use individual asperity models and neglect coupling between their strain fields, as shown below.

In the analysis given above, each crest of the sinusoidal surface profile represents an asperity. In turn, the tip of a wedge placed on a flat half-space approximates an asperity as illustrated in Fig. 13. An initial stress distribution at the base of a wedge tip is estimated from the expressions for stress distribution for a full (infinite) wedge. The stresses in a wedge σ_θ , σ_r and $\tau_{r\theta}$, given in terms of polar coordinates, are [28]:

$$\frac{\pi r}{2a} (\sigma_\theta - \sigma_r) = \frac{\pi \cos \gamma \cos \theta}{\pi - 2\gamma + \sin 2\gamma} \quad (A4)$$

$$- \int_0^\infty P(\xi) \sin \{ \xi \log(a/r) \} d\xi,$$

$$\frac{\pi r}{2a} (\sigma_\theta + \sigma_r) = \frac{\pi \cos \gamma \cos \theta}{\pi - 2\gamma + \sin 2\gamma} \quad (A5)$$

$$+ \int_0^\infty [P(\xi) - \xi Q(\xi)] \frac{\sin \{ \xi \log(a/r) \}}{1 + \xi^2} d\xi$$

$$- \int_0^\infty [Q(\xi) + \xi P(\xi)] \frac{\cos \{ \xi \log(a/r) \}}{1 + \xi^2} d\xi,$$

$$\frac{\pi r}{a} \tau_{r\theta} = \int_0^\infty T(\xi) \cos \{ \xi \log(a/r) \} d\xi, \quad (A6)$$

where $P(\xi)$, $Q(\xi)$ and $T(\xi)$ are given by

$$P(\xi) = \frac{\cos(\gamma + \theta) \cosh(\pi/2 - \gamma + \theta)\xi + \cos(\gamma - \theta) \cosh(\pi/2 - \gamma - \theta)\xi}{\xi \sin 2\gamma + \sinh(\pi - 2\gamma)\xi}, \quad (A7)$$

$$Q(\xi) = \frac{\sin(\gamma + \theta) \sinh(\pi/2 - \gamma + \theta)\xi + \sin(\gamma - \theta) \sinh(\pi/2 - \gamma - \theta)\xi}{\xi \sin 2\gamma + \sinh(\pi - 2\gamma)\xi}, \quad (A8)$$

$$T(\xi) = \frac{\cos(\gamma + \theta) \sinh(\pi/2 - \gamma + \theta)\xi - \cos(\gamma - \theta) \sinh(\pi/2 - \gamma - \theta)\xi}{\xi \sin 2\gamma + \sinh(\pi - 2\gamma)\xi}, \quad (A9)$$

An iterative approach using (Eqs (A4)–(A9)) yields the combined stress–strain field of a wedge tip located on a half-space by matching boundary conditions at the base of the wedge tip and the half-space where they are attached. However, for a first-order approximation, we only match the load at the interface. Total displacement

on the wedge tip ($-\lambda/2 < x < \lambda/2$ and $0 \leq y \leq h_{asp}$) results from a combination of local wedge displacement and displacement of the half space resulting from the load on the wedge tip.

The influence coefficients calculated as described above are compared with the influence coefficients given by the classical approach. The results, presented in Fig. 13, give the difference between displacement on a smooth elastic half-space loaded over the strip $-a < x < a$ by unit pressure and one on a rough surface at an angle to the surface mean plane. This difference caused by a wedge tip is confined to within the immediate vicinity of the load suggesting that the changes in influence coefficients due to asperity slopes are primarily local and most significant within $-3a < x < 3a$.

Although the approximate analysis given above shows that conventional influence functions can be used for asperities with small slopes, this technique can be applied directly to cases where asperities have larger slopes. In such cases, only a few of the terms in the flexibility matrices need to be modified by using the technique developed here. For the range of surface topography considered in the numerical examples in this paper, the maximal asperity slope did not exceed 6.5° . Hence, the use of classical influence coefficients is permissible for calculation of rough surfaces as described above.

References

- [1] Bowden FP, Tabor D. London: Oxford University Press, 1954.
- [2] Kragelsky IV. Friction and wear. Washington: Butterworths, 1965.
- [3] Boyd J, Robertson BP. The friction properties of various lubricants at high pressures. *Trans ASME* 1945;67:51–9.
- [4] Briscoe BJ, Scruton B, Willis FR. The shear strength of thin lubricant films. *Proc Roy Soc A* 1973;333:99–114.
- [5] Gane N, Pfaelzer PF, Tabor D. Adhesion between clean surfaces at light loads. *Proc Roy Soc A* 1974;340:495–517.
- [6] Fuller KNG, Tabor D. The effect of surface roughness on the adhesion of elastic solids. *Proc Roy Soc A* 1975;345:327–42.
- [7] Kragelsky IV, Dobychin MN, Kombalov VS. Friction and wear calculation methods. New York: Pergamon Press, 1982.
- [8] Greenwood JA, Williamson JBP. Contact of nominally flat surfaces. *Proc Roy Soc A* 1966;295:300–19.
- [9] Whitehouse DJ, Archard JF. The properties of random surfaces of significance in their contact. *Proc Roy Soc A* 1970;316:97–121.
- [10] Nayak PR. Random process model of rough surfaces. *ASME J Lubr Technol* 1971;93:398–407.
- [11] Bush AW, Gibson RE, Thomas TR. The elastic contact of a rough surface. *Wear* 1975;35:87–111.
- [12] Johnson KL. Contact mechanics. Cambridge: Cambridge University Press, 1987.
- [13] Francis HA. Application of spherical indentation mechanics to reversible and irreversible contact between rough surfaces. *Wear* 1977;45:221–69.
- [14] Ogilvy JA. Numerical simulations of friction between contacting rough surfaces. *J Phys D, Appl Phys* 1991;24:2098–109.
- [15] Chang WR, Etsion I, Bogy DB. Adhesion model for metallic rough surfaces. *ASME J Trib* 1988;110:50–8.
- [16] Ernst H, Merchant ME. Surface friction of clean metals—a basic factor in the metal cutting process. In: *Proceedings Special Summer Conference on Friction and Surface Finish*, Massachusetts Inst. Technology, Cambridge, MA, 1940;76–101.
- [17] Tabor D. In: Field JE, editor. *The properties of diamond*. Oxford: Academic Press, 1979.
- [18] Ford IJ. Roughness effect on friction for multi-asperity contact between surfaces. *J Phys D, Appl Phys* 1993;26:2219–25.
- [19] Seal M. The friction of diamond. *Phil Mag A* 1981;43(3):587–94.
- [20] Suh NP, Sin HC. On genesis of friction. *Wear* 1981;69:91–114.
- [21] Bailey DM, Sayles RS. Effect of roughness and sliding friction on contact stresses. *ASME J Trib* 1991;113:729–34.
- [22] Hu Y-Z, Barber GC, Zhu D. Numerical analysis for the elastic contact of real rough surfaces. *STLE Trans* 1999;42(3):443–51.
- [23] Tworzydło WW, Cecot W, Oden JT, Yew CH. Computational micro- and macroscopic models of contact and friction: formulation. Approach and applications. *Wear* 1998;220:113–40.
- [24] Bengisu MT, Akay A. Relation of dry-friction to surface roughness. *ASME J Trib* 1997;119:18–25.
- [25] Bengisu MT, Akay A. Stick-slip oscillations: dynamics of friction and surface roughness. *J Acoust Soc Am* 1999;105(1):194–205.
- [26] Webster MN, Sayles RS. A numerical model for the elastic frictionless contact of real rough surfaces. *ASME J Trib* 1986;108:314–20.
- [27] Akai TJ. *Applied numerical methods for engineers*. New York: John Wiley and Sons Inc, 1994.
- [28] Tranter CJ. The use of the mellin transform in finding the stress distribution in an infinite wedge. *Quart J Mech Appl Math* 1948;1:125–30.
- [29] Ren N, Lee SC. Contact simulation of three-dimensional rough surfaces using moving grid method. *ASME J Trib* 1993;115:597–601.
- [30] Jiang X, Hua DY, Cheng HS, Ai X, Lee SIC. A mixed elastohydrodynamic lubrication model with asperity contact. *ASME J Trib* 1999;121:481–91.
- [31] Stanley HM, Kato T. An FFT-based method for rough surface contact. *ASME J Trib* 1997;119:481–5.
- [32] Ai X, Sawamiphakdi K. Solving elastic contact between rough surfaces as an unconstrained strain energy minimization by using CGM and FFT techniques. *ASME J Trib* 1999;121:481–91.
- [33] Greenwood JA, Tripp JH. The elastic contact of rough spheres. *ASME Trans, Series E, J Appl Mech* 1967;34:153–9.
- [34] Peklenik J. New developments in surface characterization and measurement by means of random process analysis. *Proc Inst Mech Eng* 1967;182(3):108–26.
- [35] Hu YZ, Tonder K. Simulation of 3-D random rough surface by 2-D digital filter and Fourier analysis. *Int J Mach Tools Manufact* 1992;32(1/2):83–90.
- [36] Singer IL. Solid lubrication processes. In: Singer IL, Pollock HM, editors. *Fundamentals of friction: macroscopic and microscopic processes*. Dordrecht: Kluwer, 1992:237–61.
- [37] Tian X, Bhushan B. A numerical three-dimensional model for the contact of rough surfaces by variational principle. *ASME J Trib* 1996;118:33–42.